

Patterns and driving forces of dimensionality-dependent charge density waves in $2H$ -type transition metal dichalcogenides

Dongjing Lin,¹ Shichao Li,¹ Jinsheng Wen,^{1,2} Helmuth Berger,³

László Forró,³ Huibin Zhou,^{4,5} Shuang Jia,^{4,5} Takashi Taniguchi,⁶

Kenji Watanabe,⁶ Xiaoxiang Xi,^{1,2,*} and Mohammad Saeed Bahramy^{7,8,†}

¹*National Laboratory of Solid State Microstructures and Department of Physics,
Nanjing University, Nanjing 210093, China.*

²*Collaborative Innovation Center of Advanced Microstructures,
Nanjing University, Nanjing 210093, China.*

³*Institute of Condensed Matter Physics,
École Polytechnique Fédérale de Lausanne, 1015 Lausanne, Switzerland.*

⁴*International Center for Quantum Materials,
School of Physics, Peking University, Beijing 100871, China.*

⁵*Collaborative Innovation Center of Quantum Matter, Beijing 100871, China.*

⁶*National Institute for Materials Science,
1-1 Namiki, Tsukuba 305-0044, Japan.*

⁷*Quantum-Phase Electronics Center (QPEC) and Department of Applied Physics,
The University of Tokyo, Tokyo 113-8656, Japan.*

⁸*RIKEN Center for Emergent Matter Science (CEMS), Wako 351-0198, Japan.*

Two-dimensional (2D) materials have become a fertile playground for the exploration and manipulation of novel collective electronic states. Recent experiments have unveiled a variety of robust 2D orders in highly-crystalline materials ranging from magnetism^{1,2} to ferroelectricity^{3–5} and from superconductivity⁶ to charge density wave (CDW) instability^{7,8}. The latter, in particular, appears in diverse patterns even within the same family of materials with isoelectronic species. Furthermore, how they evolve with dimensionality has so far remained elusive. Here we propose a general framework that provides a unified picture of CDW ordering in the 2H polytype of four isoelectronic transition metal dichalcogenides $2H-MX_2$ ($M=\text{Nb, Ta}$ and $X=\text{S, Se}$). We first show experimentally that whilst NbSe_2 exhibits a strongly enhanced CDW order in the 2D limit, the opposite trend exists for TaSe_2 and TaS_2 , with CDW being entirely absent in NbS_2 from its bulk to the monolayer. Such distinct behaviours are then demonstrated to be the result of a subtle, yet profound, competition between three factors: ionic charge transfer, electron-phonon coupling, and the spreading extension of the electronic wave functions. Despite its simplicity, our approach can, in essence, be applied to other quasi-2D materials to account for their CDW response at different thicknesses, thereby shedding new light on this intriguing quantum phenomenon and its underlying mechanisms.

CDWs are the ground state of some low-dimensional metals, featuring simultaneous periodic modulation of the mobile charge density and distortion of the crystal lattice⁹. Their mechanism has been under close scrutiny for decades^{10,11} and their relation with superconductivity bears important implications regarding the nature of the superconducting states^{12,13}. The advent of 2D materials¹⁴ ushers in a new era of exploring CDWs in confined dimensions^{15,16}. Mechanical exfoliation^{8,17,18}, molecular-beam epitaxy (MBE)^{7,19–21}, and chemical vapour deposition^{22,23} have produced a plethora of 2D materials exhibiting CDWs. Dimensionality reduction was shown to enhance the CDW order in some of them^{8,19,21,23} while suppress it in others^{7,18,22,24}. Even for the same compound^{7,8,19,20}, results from different studies are scattered. For better understanding and control of the CDW states, it is thus imperative to determine the key factors governing the intrinsic effects of dimensionality on CDWs.

In this work, we systematically study the CDWs in group-V transition metal dichalcogenides $2H-MX_2$ ($M=\text{Nb, Ta}$ and $X=\text{S, Se}$). We introduce a chemical-bonding framework that can explain the distinct CDW properties observed in these systems and materials alike. The prototypes chosen here all crystalize in the so-called $2Ha$ structure¹⁰ (Figure 1a). The transition metal and chalcogen atoms form an $X-M-X$ sandwich in the trigonal prismatic coordination, henceforce called a monolayer. The unit cell for the bulk crystals consists of two such monolayers rotated 180° from each other and stacked with the transition metal atoms

aligned along the c axis. Common to all these compounds is a mismatch of valency between the central M ion ($3+$) and the neighbouring chalcogens (each in $2-$ state). As such, they all show a metallic behaviour with a mixed ionic-covalent character. Figure 1a illustrates three major pathways for charge distribution in such a metallic environment: (1) an incomplete ionic charge transfer between the transition metal cation and its adjacent chalcogen anions within a monolayer (denoted as ΔQ_I and determined by their electronegativity difference, see Supplementary Section 1) forming the ionic M - X bonds; (2) intralayer axial and planar σ -electron hoppings between the chalcogen p orbitals, both forming covalent X - X bonds; (3) interlayer σ -hoppings across the van der Waals gap.

The contribution of each channel to CDWs can be assessed according to whether the formed chemical bonds make the lattice harder or softer. In principle, a harder lattice is less susceptible to distortions, hence less amenable to CDW formation. This argument suggests the reduced tendency of CDW transitions in materials with sizable ionic charge transfer, as stronger ionic bonds make the lattice more rigid. However, the spatial extent of the ionic charge transfer crucially influences the strength of the ionic bonds. For example, the electronic bandwidth of the topmost valence band in monolayer TaS₂ is nearly 140% of that for monolayer NbSe₂ (Figure 1b and 1c; for a full comparison also see Supplementary Figure S2), thereby enabling a more extended charge distribution (as compared in Figure 1d and 1e). This is ascribed to the large spin-orbit coupling of heavy tantalum atoms as well as the increased screening of the Coulomb potential from their nuclei due to their additional shells of semi-core and core states. Because of the extended charge distribution, despite the substantial total ionic charge transfer for TaS₂ shown in Figure 1f, multiple bonds are involved in this sharing. Hence, its net effect on the lattice is counteracted in favour of CDW transition. In contrast, intralayer covalency, more pronounced in Nb-based compounds, is unfavourable for CDWs, as it pins the layers to each other, and thus, hardens the whole lattice. Interlayer σ -hopping works in unison with intralayer covalent bonding to account for the dimensionality-dependent CDWs in these compounds. This complexity in charge distribution obviously hinders the predictability of CDW phase transition in general and its dependence on dimensionality, specifically. However, as we discuss later, behind such chaos there appears to be an order that can be rationalized purely based on the chemistry of metals. Before that, let us first present the characteristic CDW features that we have observed experimentally in these compounds.

High-quality single crystals were chosen for our experiments. Their temperature-dependent resistance data in Figure 2a show typical metallic behaviour, in stark contrast to the metal-insulator transition expected for Peierls instability. CDW transitions manifest as a weak hump at ~ 30 K for NbSe₂ and as clear kinks at ~ 80 K and ~ 120 K for TaS₂ and TaSe₂, respectively. NbS₂ lacks CDW order and thus does not show an anomaly in the resistance. These temperatures for the incommensurate CDW transition (T_{CDW}) as

well as the superconducting transitions at a lower temperature are consistent with those established in the literature²⁵. Atomically thin samples were mechanically exfoliated from the bulk crystals, with special care taken to minimize sample degradation (see Methods).

We used Raman scattering to obtain both CDW signatures and phonon information²⁶. Figure 2b shows room temperature Raman spectra of the bulk compounds, collected in the collinear (XX) and cross (XY) polarization configurations. In the backscattering geometry of our experiment, the former detects both A_{1g} and E_{2g} symmetry while the latter only couples to E_{2g} ⁸. Four common features are noted in the data: (1) a rigid layer mode with E_{2g} symmetry (labelled as shear mode), which corresponds to interlayer shearing vibration and distinguishes the $2H$ from $1T$ and $3R$ polytypes; (2) an A_{1g} phonon mode, which only involves the chalcogen atoms vibrating against each other along the c axis; (3) an E_{2g} phonon mode, which involves the transition metal and chalcogen atoms vibrating along opposite directions within the layer plane; (4) a broad two-phonon scattering peak commonly assigned as due to the CDW soft phonons^{26–28}. The vibration patterns for the A_{1g} and E_{2g} modes suggest that the ionic bonds dominate their eigenfrequencies. As shown in Figure 2c, both the A_{1g} and E_{2g} modes are found to have much higher frequencies in S-based $2H-MX_2$ compounds than in Se-based ones. Sulphur due to its higher electronegativity can gain more charge from the M site, thereby making the resulting M -S bond harder than its M -Se counterpart in $2H-MSe_2$. This is consistent with the trend of ionic charge transfer shown in Figure 1f.

Figure 2d compares the 300 K and 4 K spectra, with new modes emerging at low temperature in all compounds except NbS_2 . These are the amplitude modes or zone-folded modes unique to the CDW phase^{8,27,28}. The former features characteristic softening and broadening upon approaching T_{CDW} from below, while the latter shows only a minute change of the frequency. Figure 3b, d, and f show the layer number dependence of these modes at 4 K for $NbSe_2$, $TaSe_2$, and TaS_2 , respectively. We focus on the amplitude modes, which are the most pronounced features in the spectra below 100 cm^{-1} . $NbSe_2$ exhibits a single broad peak that shifts from below 50 cm^{-1} in the bulk to 73 cm^{-1} in the monolayer, while the intensity is less affected. In contrast, both $TaSe_2$ and TaS_2 exhibit multiple sharper amplitude modes below 100 cm^{-1} . Each peak shows a weak layer number dependence for its frequency, while the intensity dramatically diminishes in atomic layers. The blueshift of the mode frequency (suppression of the mode intensity) correlates well with enhanced (reduced) T_{CDW} in atomically thin $NbSe_2$ ($TaSe_2$ and TaS_2), as will be detailed below. The completely different behaviours of the amplitude modes in the Nb- and Ta-based compounds call for further investigations.

We do not observe any new modes at low temperature in NbS_2 down to the monolayer (Supplementary Figure S3), therefore concluding the entire absence of CDW in this compound. Previous work has shown latent CDW in bulk NbS_2 due to the strong anharmonic-

ity of the lattice potential²⁹. Our temperature-dependent study of the A_{1g} mode frequency shows that NbS₂ indeed exhibits the largest degree of lattice anharmonicity among the four compounds (Supplementary Section 3.2). Our calculation shown in Figure 1f suggests enhanced ionic bonding upon reducing the layer number in NbS₂. CDWs, therefore, do not emerge in atomically thin samples, although a recent study predicts otherwise³⁰.

Temperature and layer-number dependent Raman measurements show systematic evolution of the amplitude modes in NbSe₂, TaS₂, and TaSe₂ (Supplementary Figure S3). To facilitate comparison of the mode intensity among different samples, we transform the raw spectra I to $I/I_0 - 1$, where I_0 is a high-temperature spectrum far above T_{CDW} . The normalized temperature-dependent Raman scattering intensity maps for samples of various thickness are shown in Figure 3a, c and e. The amplitude modes are accentuated in red, which diminish into the background upon increasing temperature. For NbSe₂, we clearly identify a strong enhancement of T_{CDW} in the bilayer and monolayer, consistent with a previous Raman study using a different excitation laser energy⁸. For TaSe₂ and TaS₂, although the mode intensity is significantly weakened in the atomically thin samples, the transition temperature appears similar to that of the bulk.

Figure 4a summarises the layer number dependence of T_{CDW} for each compound, estimated from the temperature dependence of the amplitude mode intensity, integrated with respect to a featureless background (Supplementary Section 4). The figure clearly shows enhanced (suppressed) T_{CDW} in NbSe₂ (TaSe₂ and TaS₂) when approaching the monolayer limit. The trends are further confirmed by analysing the amplitude mode frequency and the zone-folded mode intensity (Supplementary Sections 5–7). NbS₂ do not show Raman signature of CDWs for the measured bulk, bilayer, and monolayer samples, hence their vanishing T_{CDW} .

The disparate thickness-dependent T_{CDW} observed for the isostructural and isoelectronic compounds in the same material family is highly unusual. Since the significant two-phonon scattering peak in these compounds originates from the longitudinal acoustic phonon branch exhibiting Kohn anomaly^{26–28}, and because its frequency and temperature variation show rather weak thickness dependence (Supplementary Section 8), we infer a nearly thickness-independent CDW wavevector for NbSe₂, TaSe₂, and TaS₂. The thickness dependence of T_{CDW} is, therefore, not related to different forms of superlattice. Instead, it appears to originate from the intrinsic chemical properties of the ingredients, constituting these materials. First of all, the existence of CDWs in monolayer NbSe₂, TaSe₂, and TaS₂ is permitted by their incomplete ionic bonding. As we explained earlier, this is primarily due to a mismatch between the valence state of M cations and X anions. Furthermore, the occurring ionic charge transfer is either small and spatially highly localized as in the case of NbSe₂ or significant but spatially extended as in the case of TaSe₂ and TaS₂. In going from a monolayer to bulk, the nature of bonding between the layers and their effect on the spread of the wave

functions defines the fate of the CDW in each compound. If the interlayer bonding enhances the rigidity of each layer, T_{CDW} is expected to show declining behaviour, as the thickness grows. On the other hand, if it weakens the initial bonding, the result will manifest as an enhancement of CDW instability.

The parameter which quantifies either of these trends is the intralayer covalency, ΔQ_σ . We define this parameter as the differential charge at the chalcogen sites upon migration from a monolayer to a multilayer system. A positive ΔQ_σ means that the interlayer hopping has helped each chalcogen to gain more charge, thereby making the whole entity a “harder lattice”. Needless to say, a negative ΔQ_σ means the added layers have led to a “softer lattice”. Using atomic-orbital-like Wannier functions (see Methods), we have calculated ΔQ_σ for all four compounds in the bilayer and bulk configurations (Figure 1g). As can be seen, both bilayer and bulk NbSe₂ show a significant gain in ΔQ_σ , implying that their crystal structure is relatively harder than that of monolayer NbSe₂, and thus, less prone to CDW instability. We attribute this to the localized nature of wave functions in NbSe₂, mainly made up by the axial orbitals Se- p_z and Nb- d_{z^2} (see Figure 1d). In a bilayer or bulk NbSe₂, this accordingly allows a direct σ -type interlayer hopping between these orbitals, making ΔQ_σ positive. More importantly, this additional bonding acts against the A_{1g} phonon mode, resulting in a decrease in the strength of electron-phonon coupling constant λ as depicted in Supplementary Figure S14. It then becomes clear why T_{CDW} in NbSe₂ shows a negative thickness dependence.

TaS₂ and TaSe₂ behave differently. As shown in Figure 1g, both compounds have a negative ΔQ_σ with lower values found for their bulk phases. Given their extended wave functions, the only channel allowing the interlayer coupling is σ -hopping between the chalcogen p_z orbitals of neighbouring layers. As such, the initial charge residing on the chalcogen sites is partly shifted between the layers. This, in turn, leads to a softening of the original metal-chalcogen bonding and correspondingly an enhancement of CDW instability, as observed experimentally. Interestingly, the calculated ΔQ_σ for TaS₂ turns out to be more sensitive to the number of layers as compared with that obtained for TaSe₂. Logically, one then expects a higher T_{CDW} in, for example, bulk TaS₂ than in bulk TaSe₂. In reality, however, TaSe₂ exhibits a higher T_{CDW} than TaS₂ regardless of the number of the layers. To address this apparent inconsistency, we need to include another critical parameter in our consideration. That parameter is electron-phonon coupling λ . A large λ can mediate CDW more effectively than a small λ . However, this requires a proper coupling between the phonon mode eigenvalues and electronic eigenvalues. If the phonon modes, responsible for CDW instability, have relatively high frequencies, such a coupling is not well established and, hence, a relatively small λ is achieved. This is what occurs in TaS₂. As discussed earlier, for both A_{1g} and E_{2g} modes, the corresponding phonon frequencies are higher in TaS₂ than in TaSe₂ (See Figure 2c), suggesting that the former should have a smaller λ than the latter. Our first-principles

calculations for monolayer $2H\text{-}MX_2$ confirm this indeed. In fact, as shown in Figure 4b, we find that λ is always smaller in an S-based compound when compared to its Se-based counterpart. These calculated results agree well with the available λ values reported for NbSe_2 ³¹, TaS_2 and TaSe_2 ³².

In a broader context, we can again attribute this tendency to the ionic charge transfer ΔQ_I we discussed earlier, implying a trade-off between ΔQ_I and λ . In addition to these two parameters, the spatial extension of the wave functions (represented here as $1/\langle r^2 \rangle$) plays an important role. The more localized are the wave functions, the less effective become both ΔQ_I and λ . This is because it enhances the electron-electron correlation, demobilizing the carriers and so preventing the formation of any superlattice charge ordering. As a result, if λ is not large enough, CDW remains forbidden. This then solves the last piece of the puzzle, i.e. why NbS_2 is so robust against CDW instability. We note that van Loon et al. have already given a detailed account for the competing nature of electron-phonon coupling versus the short- and long-range electron Coulomb interaction, and its prominent role in the absence of CDW instability in NbS_2 ³³. Interestingly, they suggest that the interplay between these parameters strongly enhances both charge and spin susceptibilities in NbS_2 , meaning that it is at the verge of collapsing to a CDW or even a spin density wave phase, if sufficient perturbations are introduced (for example via local magnetic impurities)³³. As such, NbS_2 appears to be an ideal candidate for exploring thermal and quantum fluctuations.

Altogether, the three parameters (1) ionic charge transfer, (2) electron-phonon coupling, and (3) the spatial extension of the electronic wave functions are the key components defining the fate of CDW ordering and its thickness dependence in this and potentially other layered materials. Thus, they can be used to create a unified phase diagram describing such instabilities in low-dimensional limits. We have schematically illustrated such a phase diagram in Figure 4c. As can be seen, the interplay between these three parameters is expected to form an abyss-like shape, deepening at regions with low ΔQ_I and λ and high $1/\langle r^2 \rangle$. Above the surface of the resulting terrain is a parameter-space within which the CDW is forbidden and below it is where CDW is allowed to emerge. We also have shown the schematic location of each of the $2H\text{-}MX_2$ compounds, studied here. Obviously, NbS_2 is the only member of this family appearing in a region at which CDW is prohibited.

Lastly, we address some controversies in the studies of 2D CDWs in NbSe_2 , TaSe_2 , and TaS_2 . For NbSe_2 , a strongly enhanced T_{CDW} from ~ 33 K in the bulk to ~ 145 K in the monolayer was previously reported in mechanically exfoliated samples on sapphire substrates⁸ and confirmed here. This is in stark contrast to the almost unchanged T_{CDW} in MBE-grown monolayer NbSe_2 on bilayer graphene⁷. For TaSe_2 , we found a rather weak suppression of T_{CDW} in the exfoliated monolayer, while MBE-grown monolayer TaSe_2 on bilayer graphene shows slightly enhanced T_{CDW} with respect to its bulk value²¹. The exfoliated samples are expected to exhibit intrinsic CDW properties, verified by control experiments on suspended

thin flakes (Supplementary Section 10). The MBE-grown samples may be affected by charge transfer from the underlying graphene substrate. For monolayer NbSe₂, such charge transfer can increase the intralayer covalency and suppress the strongly enhanced T_{CDW} . For monolayer TaSe₂, due to its extended charge distribution, charge transfer tends to accumulate between TaSe₂ and graphene, so that the intralayer covalency is reduced; CDW is therefore enhanced. CDWs were found to be absent in epitaxial monolayer TaS₂ on gold substrate³⁴, clearly deviating from the intrinsic properties found in the exfoliated TaS₂ studied here. This is again due to the charge transfer from the substrate.

In conclusion, our chemical-bonding framework provides an intuitive guide for boosting T_{CDW} , which is essential for developing CDW-based devices for applications. It may also be applied to explain the distinct dimensionality effects in the growing family 2D CDW materials³⁵. Future work should address the connection of the current framework with the existing theories for CDWs, for instance, Fermi-surface nesting and momentum-dependent electron-phonon coupling^{11,36}.

* xxi@nju.edu.cn

† bahramy@ap.t.u-tokyo.ac.jp

- ¹ Gong, C. *et al.* Discovery of intrinsic ferromagnetism in two-dimensional van der waals crystals. *Nature* **546**, 265–269 (2017).
- ² Huang, B. *et al.* Layer-dependent ferromagnetism in a van der waals crystal down to the monolayer limit. *Nature* **546**, 270–273 (2017).
- ³ Chang, K. *et al.* Discovery of robust in-plane ferroelectricity in atomic-thick SnTe. *Science* **353**, 274–278 (2016).
- ⁴ Liu, F. *et al.* Room-temperature ferroelectricity in CuInP₂S₆ ultrathin flakes. *Nat. Commun.* **7**, 12357 (2016).
- ⁵ Fei, Z. *et al.* Ferroelectric switching of a two-dimensional metal. *Nature* **560**, 336–339 (2018).
- ⁶ Saito, Y., Nojima, T. & Iwasa, Y. Highly crystalline 2D superconductors. *Nat. Rev. Mat.* **2**, 16094 (2016).
- ⁷ Ugeda, M. M. *et al.* Characterization of collective ground states in single-layer NbSe₂. *Nat. Phys.* **12**, 92 (2016).
- ⁸ Xi, X. *et al.* Strongly enhanced charge-density-wave order in monolayer NbSe₂. *Nat. Nanotech.* **10**, 765 (2015).
- ⁹ Grüner, G. *Density Waves in Solids*. Advanced book program: Addison-Wesley (Perseus Books Group, 2000).
- ¹⁰ Wilson, J. A., Di Salvo, F. J. & Mahajan, S. Charge-density waves and superlattices in the metallic layered transition metal dichalcogenides (reprinted from *Adv. Phys.*, 32, 882, (1974)).

- Adv. Phys.* **50**, 1171–1248 (2001).
- ¹¹ Rossnagel, K. On the origin of charge-density waves in select layered transition-metal dichalcogenides. *J. Phys.: Condens. Matter* **23**, 213001 (2011).
 - ¹² Fradkin, E., Kivelson, S. A. & Tranquada, J. M. Colloquium: Theory of intertwined orders in high temperature superconductors. *Rev. Mod. Phys.* **87**, 457–482 (2015).
 - ¹³ Chen, C.-W., Choe, J. & Morosan, E. Charge density waves in strongly correlated electron systems. *Rep. Prog. Phys.* **79**, 084505 (2016).
 - ¹⁴ Novoselov, K. S. *et al.* Two-dimensional atomic crystals. *Proc. Natl. Acad. Sci.* **102**, 10451–10453 (2005).
 - ¹⁵ Calandra, M., Mazin, I. I. & Mauri, F. Effect of dimensionality on the charge-density wave in few-layer 2H-NbSe₂. *Phys. Rev. B* **80**, 241108 (2009).
 - ¹⁶ Ge, Y. & Liu, A. Y. Effect of dimensionality and spin-orbit coupling on charge-density-wave transition in 2H-TaSe₂. *Phys. Rev. B* **86**, 104101 (2012).
 - ¹⁷ Hajiyeve, P., Cong, C., Qiu, C. & Yu, T. Contrast and Raman spectroscopy study of single- and few-layered charge density wave material: 2H-TaSe₂. *Sci. Rep.* **3**, 2593 (2013).
 - ¹⁸ Yu, Y. J. *et al.* Gate-tunable phase transitions in thin flakes of 1T-TaS₂. *Nat. Nanotech.* **10**, 270–276 (2015).
 - ¹⁹ Chen, P. *et al.* Charge density wave transition in single-layer titanium diselenide. *Nat. Commun.* **6**, 8943 (2015).
 - ²⁰ Sugawara, K. *et al.* Unconventional charge-density-wave transition in monolayer 1T-TiSe₂. *ACS Nano* **10**, 1341–1345 (2016).
 - ²¹ Ryu, H. *et al.* Persistent charge-density-wave order in single-layer TaSe₂. *Nano Lett.* **18**, 689–694 (2018).
 - ²² Fu, W. *et al.* Controlled synthesis of atomically thin 1T-TaS₂ for tunable charge density wave phase transitions. *Chem. Mat.* **28**, 7613–7618 (2016).
 - ²³ Wang, H. *et al.* Large-area atomic layers of the charge-density-wave conductor TiSe₂. *Adv. Mat.* **30**, 1704382 (2018).
 - ²⁴ Yang, Y. *et al.* Enhanced superconductivity upon weakening of charge density wave transport in 2H-TaS₂ in the two-dimensional limit. *Phys. Rev. B* **98**, 035203 (2018).
 - ²⁵ Naito, M. & Tanaka, S. Electrical transport properties in 2H-NbS₂, -NbSe₂, -TaS₂ and -TaSe₂. *J. Phys. Soc. Jpn.* **51**, 219–227 (1982).
 - ²⁶ Sugai, S. Lattice vibrations in the charge-density-wave states of layered transition metal dichalcogenides. *phys. stat. sol. (b)* **129**, 13–39 (1985).
 - ²⁷ Hill, H. M. *et al.* Phonon origin and lattice evolution in charge density wave states. *Phys. Rev. B* **99**, 174110 (2019).
 - ²⁸ Joshi, J. *et al.* Short-range charge density wave order in 2H-TaS₂. *Phys. Rev. B* **99**, 245144 (2019).

- ²⁹ Leroux, M. *et al.* Anharmonic suppression of charge density waves in 2H-NbS₂. *Phys. Rev. B* **86**, 155125 (2012).
- ³⁰ Bianco, R., Errea, I., Monacelli, L., Calandra, M. & Mauri, F. Quantum enhancement of charge density wave in NbS₂ in the two-dimensional limit. *Nano Letters* **19**, 3098–3103 (2019).
- ³¹ Zheng, F. & Feng, J. Electron-phonon coupling and the coexistence of superconductivity and charge-density wave in monolayer NbSe₂. *Phys. Rev. B* **99**, 161119 (2019).
- ³² Hinsche, N. F. & Thygesen, K. S. Electronphonon interaction and transport properties of metallic bulk and monolayer transition metal dichalcogenide TaS₂. *2D Mater.* **5**, 015009 (2017).
- ³³ van Loon, E. G. C. P., Rösner, M., Schönhoff, G., Katsnelson, M. I. & Wehling, T. O. Competing Coulomb and electronphonon interactions in NbS₂. *npj Quantum Mater.* **3**, 32 (2018).
- ³⁴ Sanders, C. E. *et al.* Crystalline and electronic structure of single-layer TaS₂. *Phys. Rev. B* **94**, 081404 (2016).
- ³⁵ Hossain, M. *et al.* Recent advances in two-dimensional materials with charge density waves: Synthesis, characterization and applications. *Crystals* **7**, 298 (2017).
- ³⁶ Johannes, M. D. & Mazin, I. I. Fermi surface nesting and the origin of charge density waves in metals. *Phys. Rev. B* **77**, 165135 (2008).
- ³⁷ Perdew, J. P., Burke, K. & Ernzerhof, M. Generalized gradient approximation made simple. *Phys. Rev. Lett.* **77**, 3865–3868 (1996).
- ³⁸ Giannozzi, P. *et al.* Advanced capabilities for materials modelling with Quantum ESPRESSO. *J. Phys.: Condens. Matter* **29**, 465901 (2017).
- ³⁹ Giannozzi, P. *et al.* QUANTUM ESPRESSO: A modular and open-source software project for quantum simulations of materials. *J. Phys.: Condens. Matter* **21**, 395502 (2009).
- ⁴⁰ QUANTUM ESPRESSO program package. version 6.3 (2018). URL <http://www.quantum-espresso.org/>.
- ⁴¹ Quantum ESPRESSO pseudopotential data base. URL <http://www.quantum-espresso.org/pseudopotentials>.
- ⁴² Souza, I., Marzari, N. & Vanderbilt, D. Maximally localized Wannier functions for entangled energy bands. *Phys. Rev. B* **65**, 035109 (2001).
- ⁴³ Mostofi, A. A. *et al.* wannier90: A tool for obtaining maximally-localised Wannier functions. *Comput. Phys. Commun.* **178**, 685–699 (2008).

Methods

Sample preparation. Bulk single crystals were synthesized by the chemical vapour transport method. Atomically thin flakes were mechanically exfoliated from the bulk crystals on silicone elastomer polydimethylsiloxane stamps and transferred on sapphire substrates for Raman study. To minimize sample degradation, we prepared them in a glove box filled with nitrogen gas, followed by encapsulation with thin h-BN. The flake thickness was determined

by the shear mode frequency in the Raman data (Supplementary Section 3.1).

Characterizations. Temperature dependent Raman scattering measurements were performed using a home-built confocal optical setup, consisting mainly of a Montana Instruments Cryostation and a Princeton Instruments grating spectrograph quipped with a liquid-nitrogen-cooled charge coupled device. Beam from a diode-pumped 532 nm laser was focused on the sample using a 40 \times microscope objective. The backscattered light was collected using the same objective followed by a couple of Bragg notch filters, achieving a minimum cutoff of 15 cm⁻¹ in the collinear polarization configuration. The sample chamber was evacuated to high vacuum better than 10⁻⁴ Pa throughout the experiment. Rapid temperature control was achieved using an Agile Temperature Sample Mount. To minimize laser heating, the incident power was kept below 0.1 mW for bulk samples and below 0.3 mW for thin flakes, and anti-Stokes lines were confirmed to be absent at the base temperature. Four-probe resistance measurements on the bulk crystals were conducted in an Oxford Instruments TeslatronPT system using the standard lock-in method.

Calculations. The electronic structure of 2H-MX₂ monolayers was calculated within density functional theory (DFT) using Perdew-Burke-Ernzerhof exchange-correlation functional³⁷ as implemented in Quantum Espresso program package³⁸⁻⁴⁰. We used the norm-conserving pseudo-potentials⁴¹ and plane-wave basis set with cut-off energy of 75 Ry. The relativistic effects, including spin-orbit coupling, were fully considered. The Brillouin zone was sampled by a 24 \times 24 \times 1 *k*-mesh. The ionic charge transfer and hopping parameters were obtained by constructing a 22-band tight-binding model by downfolding the DFT Hamiltonian using maximally localized Wannier functions^{42,43}. The *M*-3*d* and *X*-*p* atomic orbitals were taken as projection centres.

For the calculation of phonon modes and the corresponding electron-phonon coupling parameters, we first fully optimized both the lattice parameters and atomic positions until the magnitude of the force on each ionic site was less than 10⁻⁵ Ry/Bohr and the total energy is converged below 10⁻¹⁰ Ry. To avoid the negative phonon modes, resulting in an overestimation of λ , the Methfessel-Paxton smearing scheme with a relatively large broadening parameter $\sigma = 0.03$ Ry was used, as suggested in Ref.³¹. The dynamical matrix was then calculated based on density-functional perturbation theory employing an 8 \times 8 \times 1 *q*-mesh. Finally, we computed λ using the interpolation scheme implemented in Quantum Espresso⁴⁰.

Acknowledgements

This work was support by the National Natural Science Foundation of China (Grant Nos. 11774151, 11822405 and 11674157), the National Key Research and Development Program of China (Grant Nos. 2018YFA0307000 and 2017YFA0303201), the Natural Science Foundation of Jiangsu Province (Grant No. BK201800006) and Japan Science and Tech-

nology Agency (CREST, JST, Grant No. JPMJCR16F1). The work in Lausanne was supported by the Swiss National Science Foundation. The crystal growth in Peking University was supported by the National Natural Science Foundation of China (Grant Nos. U1832214 and 11774007) and the National Key Research and Development Program of China (2018YFA0305601). Growth of hexagonal boron nitride crystals was supported by the Elemental Strategy Initiative conducted by the MEXT, Japan and the CREST (JPMJCR15F3), JST.

Author contributions

X.X. and M.S.B. conceived the project. D.L. and X.X. performed the experiments. S.L., J.W., H.B., L.F., H.Z. and S.J. contributed the transition metal dichalcogenides crystals. T.T. and K.W. grew the h-BN crystals. D.L. and X.X. analysed the experimental data. M.S.B. performed the first-principles calculations. X.X. and M.S.B. interpreted the results and co-wrote the paper, with comments from all authors.

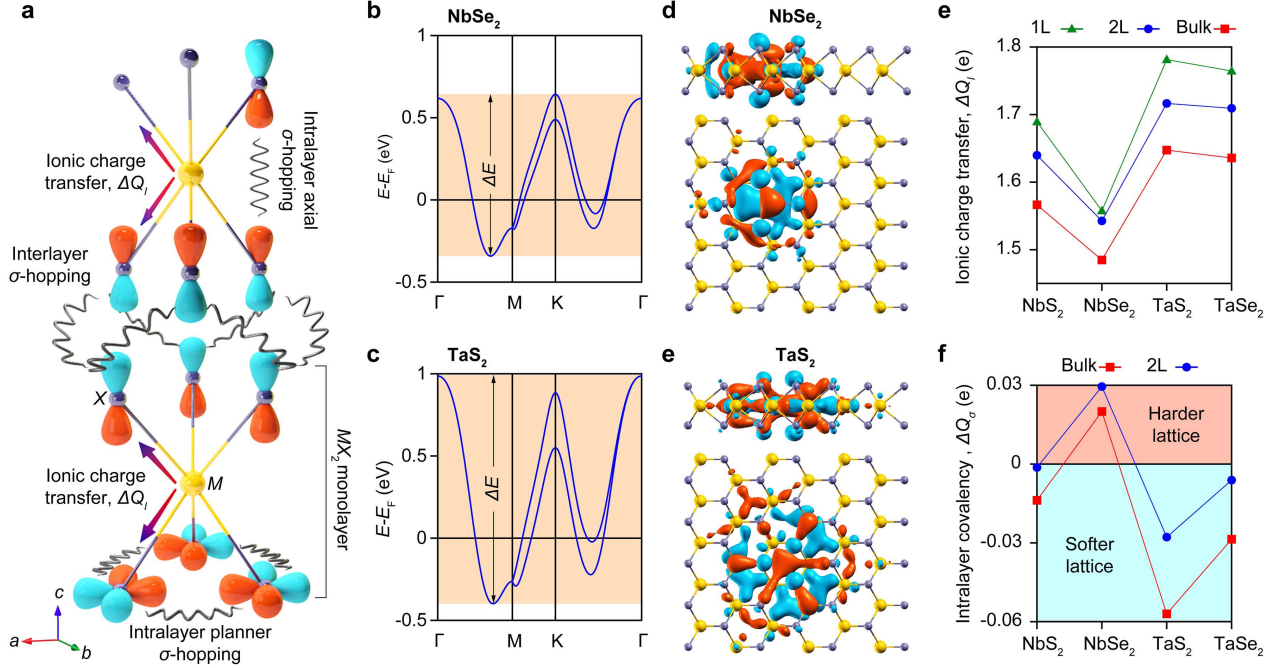


Figure 1. **Chemical bonding mechanism in $2H\text{-MX}_2$ ($M=\text{Nb, Ta}$ and $X=\text{S, Se}$).** **a**, Schematic illustration of the charge transfer channels, including intralayer ionic charge transfer ΔQ_I , intralayer covalent bonding (axial σ -hopping and planner σ -hopping), and interlayer σ -hopping. **b** and **c**, Electronic band structure for monolayer NbSe_2 and TaS_2 from first-principles calculations. ΔE denotes the bandwidth. **d** and **e**, calculated charge distribution in monolayer NbSe_2 and TaS_2 , viewed along the in-plane and out-of-plane directions. Orange and blue represents positive and negative signs of the electronic wave functions, respectively. **f** and **g**, Layer number dependence of the ionic charge transfer ΔQ_I and the change of the intralayer covalency ΔQ_σ upon increasing the layer number from a monolayer for all compounds.

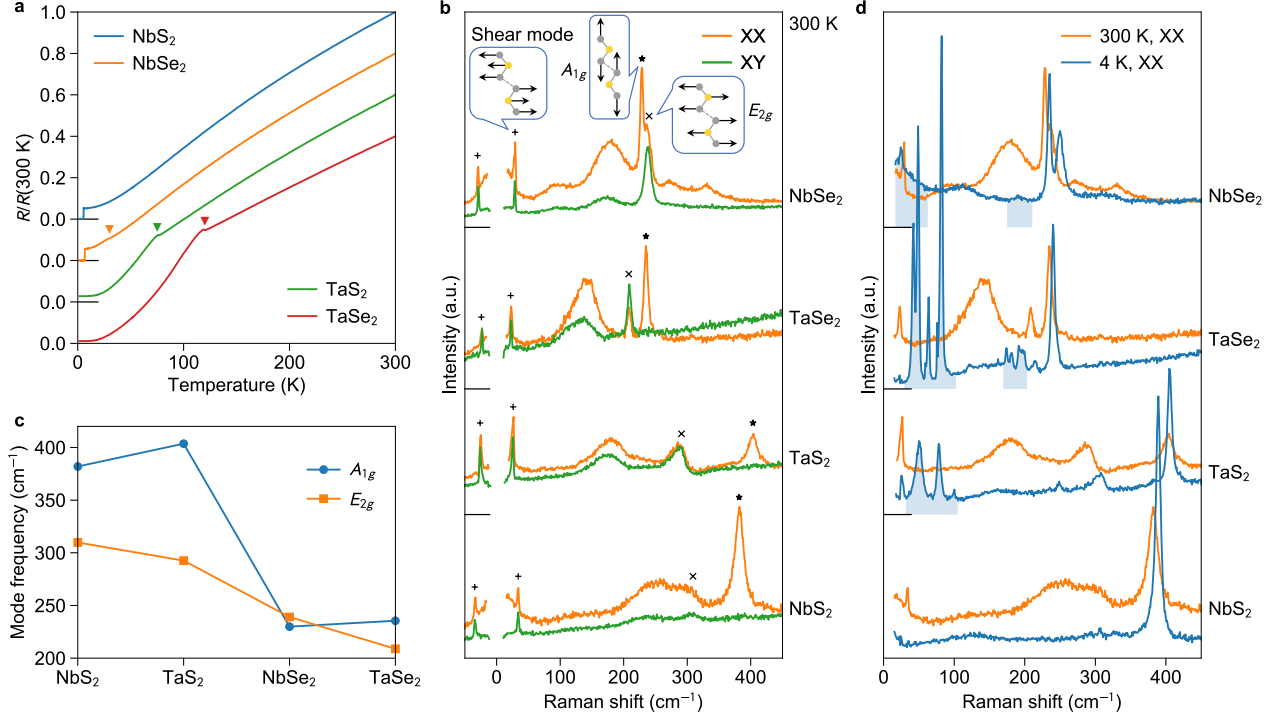


Figure 2. **Characterizations of phonon modes in high-quality bulk $2H-MX_2$ ($M=\text{Nb, Ta}$ and $X=\text{S, Se}$) samples.** **a**, Temperature dependence of the electrical resistance for all compounds, normalized to their respective values at 300 K. The triangles mark the anomalies due to CDW transitions. **b**, Raman spectra for all compounds collected in the collinear (XX) and cross (XY) polarization configurations at 300 K. The first-order phonon scattering peaks are indicated by + for the shear modes (Stokes and anti-Stokes), \times for the E_{2g} modes, and \star for the A_{1g} modes. The corresponding displacement patterns are illustrated in the balloons. **c**, Compound dependence of the A_{1g} and E_{2g} mode frequencies analyzed by peak fitting of the data in **b**. **d**, Comparison of the Raman spectra at 300 K and 4 K for the collinear polarization configuration for all compounds. CDW-induced modes are highlighted by the shaded regions. Data in **a**, **b**, and **d** are shifted vertically for clarity, with the new origins located at the crossings of the left axes and the long horizontal bars.

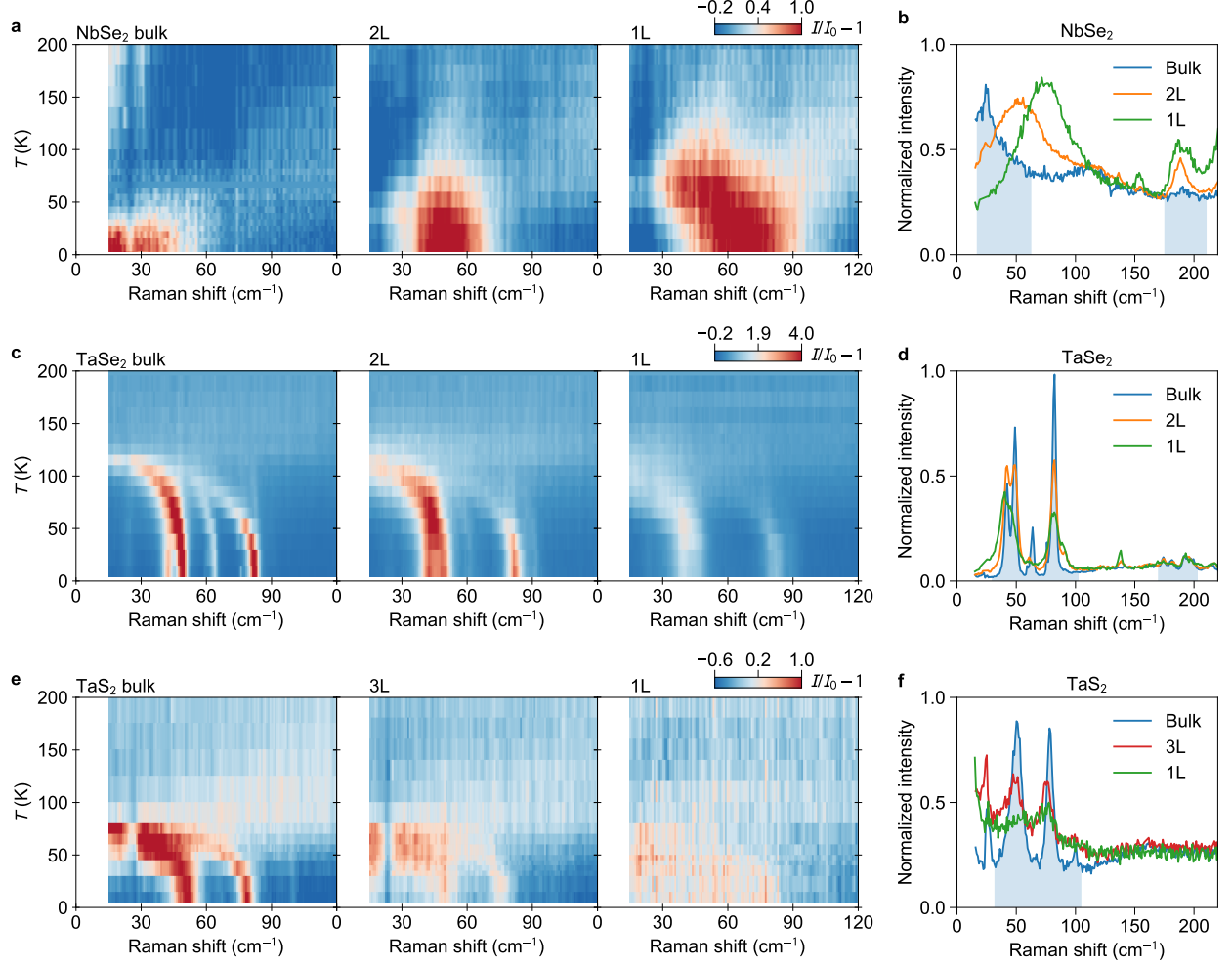


Figure 3. **Raman signature of CDW transitions in NbSe_2 , TaSe_2 , and TaS_2 .** a, c, e, Temperature dependent Raman scattering intensity maps for the three compounds with different thickness, all collected in the collinear polarization configuration. To compare different samples, each set of raw data I are normalized to a corresponding high-temperature spectrum I_0 far above T_{CDW} , and unity is subtracted from the ratio to yield $I/I_0 - 1$. b, d, f, Comparison of the Raman scattering spectra at 4 K for samples of different thickness. In each panel, the spectra are normalized to match their background intensity between $150\text{--}220\text{ cm}^{-1}$.

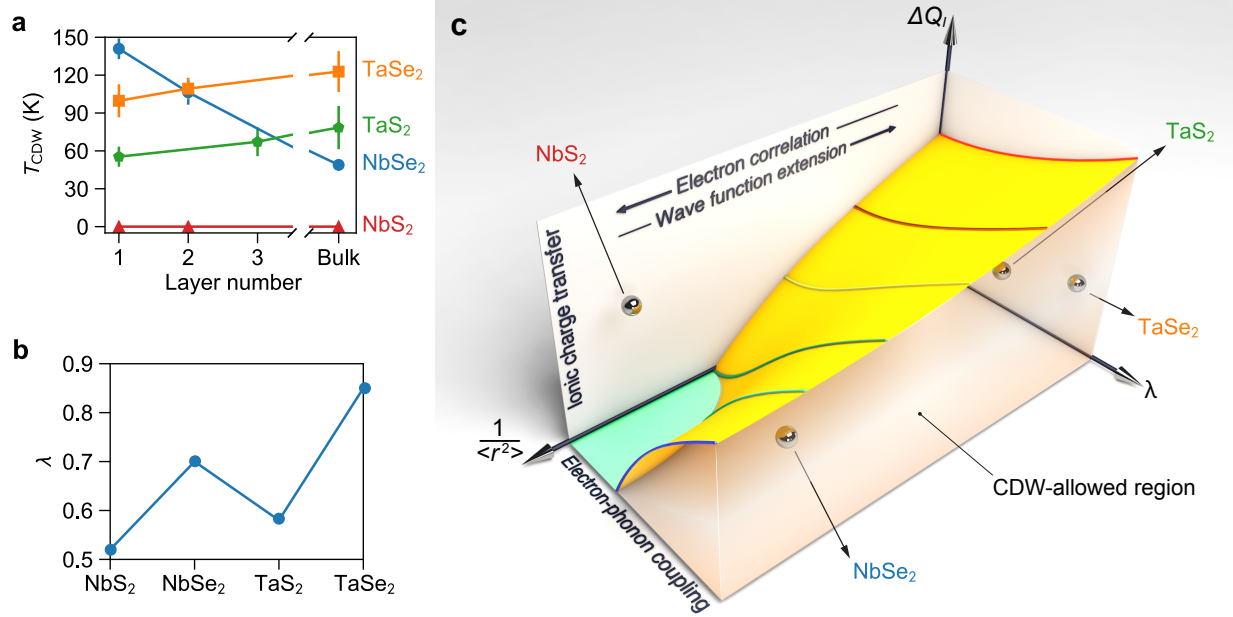


Figure 4. **Thickness dependence of T_{CDW} for $2H\text{-MX}_2$ ($M=\text{Nb}$, Ta and $X=\text{S}$, Se).** **a**, Layer-number dependence of T_{CDW} for all compounds. **b**, The calculated values of electron-phonon coupling constant λ for monolayer $1H\text{-MX}_2$. **c**, Schematic illustration of the possible phase diagram describing the CDW response in a layered material in terms of ionic charge transfer ΔQ_I , electron-phonon coupling constant λ and the spatial extension of electronic wave functions $1/\langle r^2 \rangle$.